Optical Materials 34 (2012) 1155–1160

Contents lists available at SciVerse ScienceDirect

Optical Materials

journal homepage: www.elsevier.com/locate/optmat

Fabrication and spectroscopic characterization of Ce^{3+} doped $Sr_2Y_8(SiO_4)_6O_2$ translucent ceramics

Yiqiang Shen [a], Rui Chen [b], Gagik G. Gurzadyan [b], Jinling Xu [c], Handong Sun [b], Khiam Aik Khor [c], Zhili Dong [a,*]

[a] Division of Materials Science, School of Materials Science and Engineering, Nanyang Technological University, Singapore 639798, Singapore
[b] Division of Physics and Applied Physics, School of Physical and Mathematical Sciences, Nanyang Technological University, Singapore 637371, Singapore
[c] School of Mechanical and Aerospace Engineering, Nanyang Technological University, Singapore 639798, Singapore

ARTICLE INFO

Article history:
Received 6 September 2011
Received in revised form 12 January 2012
Accepted 17 January 2012
Available online 9 February 2012

Keywords:
Translucent ceramics
Spark plasma sintering
Photoluminescence spectra
Energy transfer
Decay profile

ABSTRACT

Ce^{3+} doped $Sr_2Y_8(SiO_4)_6O_2$ translucent ceramics were successfully fabricated by spark plasma sintering and their photoluminescent properties were studied in correlation with the crystal structure. There are two crystallographic sites A^I and A^{II} for Ce^{3+} in the $Sr_2Y_8(SiO_4)_6O_2$ host and according to the analysis of the photoluminescence spectra, the energy levels of Ce^{3+} at A^I and A^{II} sites were demonstrated by the configurational coordinate model. The spectroscopic characteristics also indicated that the energy transfer from Ce^{3+} at A^I to those at A^{II} occurred. This energy transfer became more pronounced with higher Ce^{3+} doping concentration, which is confirmed by the analysis of decay profiles.

1. Introduction

The transparent and translucent ceramics have great potentials to replace their single crystal counterparts and apply as the laser medium and scintillators due to the easier fabrication process and better mechanical properties [1–3]. Ceramics usually consist of randomly oriented grains and in order to fabricate transparent ceramics, the light scattering centers including pores, impurity phases, rough surfaces and grain boundaries must be minimized or eliminated [4]. The scattering by impurity phases can be excluded by using pure raw materials. The scattering at surfaces can be suppressed by careful polishing. To eliminate the pores in the ceramic, advanced sintering methods such as hot pressing, [5] hot isostatic pressing [6] and vacuum sintering [7] is necessary. More recently, another sintering technique – spark plasma sintering (SPS) drew more attention due to its rapid heating rate and the combination of mechanical pressure, higher vacuum and electric field during sintering [8]. The scattering at grain boundaries is mainly due to the birefringence effect, which results from the different refractive indexes of the grains at both sides of the boundary [9]. Therefore, the pore-free ceramics in non-cubic crystal structures, whose refractive indexes are anisotropic, always have lower transmittance than those with cubic structures and appear translucent. Previous study about spark plasma sintered silicate oxyapatites with a hexagonal crystal structure has shown that the pores in these ceramics can scatter the incident light much more severely than the birefringence [10]. Therefore, translucent ceramics of silicate oxyapatites can be produced by suppressing the pores.

In the aspect of applications, translucent ceramics of Ce^{3+}:Lu_2SiO_5, Ce^{3+}:$SrHfO_3$ and Eu^{3+}:Lu_2O_3 have been produced and demonstrated prospective applications as scintillators [11–15]. All these ceramics have been fabricated by hot pressing technique or vacuum sintering but the time-efficient spark plasma sintering. Moreover, very few studies on ceramic forms of Ce^{3+} doped silicate apatites have been reported since single crystals of Ce^{3+} doped silicate oxyapatites were grown and used in scintillators for X- and gamma-radiation [16]. Based on our previous studies [10], it is believed that Ce^{3+} doped silicate apatite translucent ceramics can be fabricated by SPS sintering as well. The present work reports the SPS processing of these translucent ceramics, followed by a detailed study on their photoluminescent properties.

2. Experimental

Silicate oxyapatites $Sr_2Y_{8-x}Ce_x(SiO_4)_6O_2$ ($x = 0.01$, 0.05 and 0.1) powders were prepared through solid state reaction. Stoichiometric amount of $SrCO_3$ (>99.0%, Alfa Aesar), silica gel 60 (>99.0%, Fluka), CeO_2 (>99.95%, Sigma–Aldrich) and synthetic nano-sized Y_2O_3 were

* Corresponding author.
E-mail addresses: SHEN0061@ntu.edu.sg (Y. Shen), CHEN0529@ntu.edu.sg (R. Chen), GURZADYAN@ntu.edu.sg (G.G. Gurzadyan), JLXU@ntu.edu.sg (J. Xu), HDSUN@ntu.edu.sg (H. Sun), MKAKHOR@ntu.edu.sg (M. Khor), ZLDONG@ntu.edu.sg (Z. Dong), ZLDONG@ntu.edu.sg (Z. Dong).

0925-3467/$ - see front matter © 2012 Elsevier B.V. All rights reserved.
doi:10.1016/j.optmat.2012.01.020

weighted stoichiometrically to give 4 g for each batch. The nano-sized Y_2O_3 powder was synthesized from precipitation method and the details were described elsewhere [17]. The powders were mixed for 12 h using a horizontal ball milling machine with ZrO_2 balls and ethanol, and the resultant slurry was dried at 70 °C overnight in oven, followed by a solid state reaction at 1400 °C for 6 h in a tube furnace with reduced atmosphere (95% N_2 + 5% H_2).

The resultant powders were further ball milled using zirconia balls and ethanol for 6 h. A SPS system (Sumitomo Coal Mining SPS system, Dr. Sinter Modal 1050, Japan) was used to prepare the consolidated ceramics. Two grams powder was placed in a graphite die and aligned in the SPS chamber. The sample was first heated to 600 °C with a heating rate of 300 °C/min and held for 1 min for stabilization. After that the temperature was increased to the sintering temperature with a heating rate of 100 °C/min and dwelled for 3 min. During the whole process, the pressure applied on the graphite die was kept at 23 MPa and the temperature profile was monitored by a pyrometer. The as-received ceramic pellets were heat treated at 1200 °C for 1 h in a muffle furnace to remove the residual carbon on the surface as well as other defects. In order to minimize the amount of oxidized cerium cations, the pellets were heated at 1200 °C for 2 h in a tube furnace with reduced atmosphere. The surfaces of the two pellets were carefully polished by sand papers and diamond pastes to a thickness of about 1 mm. The densities were measured by Archimedes methods.

The phase compositions of the as-synthesized samples were studied by X-ray diffraction (XRD). The data were collected using the Shimadzu 6000 X-ray diffractometer with Cu Kα radiation. The machine was operated at 40 kV and 40 mA with a 2θ step size of 0.02° and a scan rate of 2°/min. The morphologies were observed using a JEOL JSM-6340F scanning electron microscope (SEM, Tokyo, Japan) with a field emission source. The photoluminescent (PL) and photoluminescent excitation (PLE) measurements were carried out using a Shimadzu RF-5301PC spectrophotometer.

Time-resolved photoluminescence (TRPL) was carried out at room temperature by time-correlated single photon counting (TCSPC) technique, with a resolution of 10 ps (PicoQuant PicoHarp 300), and the 295 nm pulse laser (100 fs, 80 MHz) from the third harmonic of the titanium sapphire laser (Chameleon, Coherent Inc.) was used as an excitation source.

3. Results and discussion

The morphology of ball-milled $Sr_2Y_{7.99}Ce_{0.01}(SiO_4)_6O_2$ powders, which is typical for all the Ce:$Sr_2Y_8(SiO_4)_6O_2$ samples, is shown in

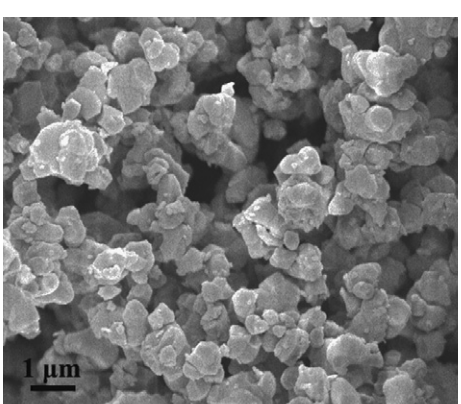

Fig. 1. The morphology of ball-milled $Sr_2Y_{7.99}Ce_{0.01}(SiO_4)_6O_2$ powders, which is typical for all the Ce^{3+}:$Sr_2Y_8(SiO_4)_6O_2$ samples. The powders are homogeneous with sub-micrometer sizes.

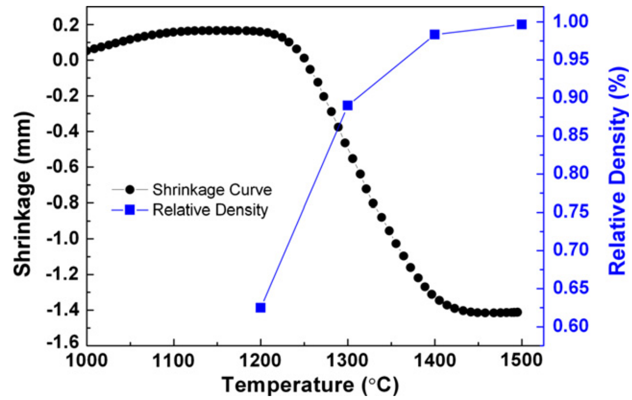

Fig. 2. The displacement curve of $Sr_2Y_{7.99}Ce_{0.01}(SiO_4)_6O_2$ ceramic during SPS (●), which is typical for all the Ce^{3+}:$Sr_2Y_8(SiO_4)_6O_2$ samples. The relative densities from the samples sintered at different temperatures are also indicated (■).

Fig. 1. The powders are homogeneous with sub-micrometer sizes, ensuring a high sinterability during the spark plasma sintering.

The displacement curve of $Sr_2Y_{7.99}Ce_{0.01}(SiO_4)_6O_2$ ceramic during SPS are shown in Fig. 2. The shrinkage process begins at about 1200 °C and continues until the temperature is raised to 1500 °C. No further shrinkage is observed in dwell regions in sintering curves. The other two samples $Sr_2Y_{7.95}Ce_{0.05}(SiO_4)_6O_2$ and $Sr_2Y_{7.9}Ce_{0.1}(SiO_4)_6O_2$ also have similar sintering behaviors. The relative densities from the samples sintered at different temperatures are also indicated in Fig. 2, and the values for all the ceramics sintered at 1500 °C reaches about 99.7%.

The appearances of $Sr_2Y_{8-x}Ce_x(SiO_4)_6O_2$ (x = 0.01, 0.05 and 0.1) translucent ceramics with thickness of 1 mm are shown in Fig. 3a and the pattern beneath can be well displayed. A typical SEM image of the sample surface is shown in Fig. 3b. It indicates that the ceramic is well densified by the sintering process and no entrapped pores are observed.

XRD patterns of $Sr_2Y_{8-x}Ce_x(SiO_4)_6O_2$ (x = 0.01, 0.05 and 0.1) translucent ceramics and the reference pattern of $Sr_2Y_8(SiO_4)_6O_2$ generated from the refinement are shown in Fig. 4. The ceramics are all pure apatite phases and no peaks from impurities are detected. Enlarged patterns show that the XRD peaks shift to the lower 2θ values with the increase of Ce^{3+} content, indicating that

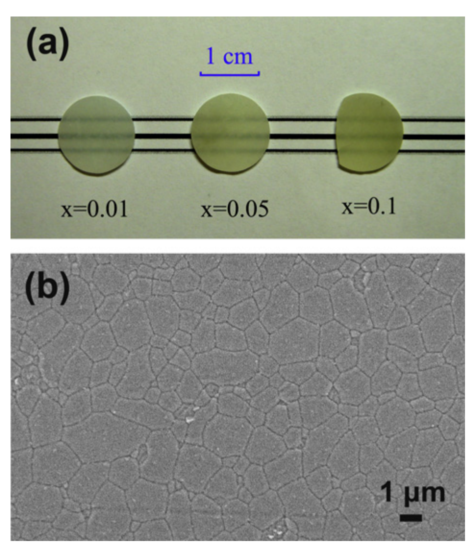

Fig. 3. (a) The appearances of $Sr_2Y_{7.99}Ce_{0.01}(SiO_4)_6O_2$ (left), $Sr_2Y_{7.95}Ce_{0.05}(SiO_4)_6O_2$ (middle) and $Sr_2Y_{7.9}Ce_{0.1}(SiO_4)_6O_2$ (right) ceramics with thickness about 1 mm. (b) A typical SEM image from polished sample surface. All grains are closely compacted and no pores are observed.

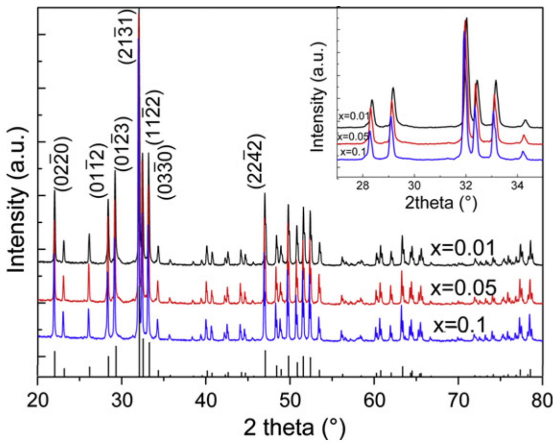

Fig. 4. XRD for $Sr_2Y_{7.99}Ce_{0.01}(SiO_4)_6O_2$ (black), $Sr_2Y_{7.95}Ce_{0.05}(SiO_4)_6O_2$ (red) and $Sr_2Y_{7.9}Ce_{0.1}(SiO_4)_6O_2$ (blue). The XRD intensities of $Sr_2Y_8\ (SiO_4)_6O_2$ from refinement is indicated at the bottom. The inset is the enlarged image in the 2θ range from 27° to 35°. The peaks are shifted to lower 2θ values when the Ce^{3+} doping concentration is increased.(For interpretation of the references to colour in this figure legend, the reader is referred to the web version of this article.)

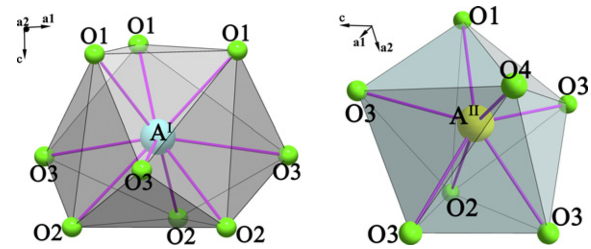

Fig. 5. The polyhedral descriptions of A^I and A^{II} sites in Ce^{3+}:$Sr_2Y_8(SiO_4)_6O_2$. A^I–O polyhedron (left) has a tricapped trigonal-prismatic geometry and A^{II}–O (right) polyhedron has a pentagonal bipyramidal geometry. Blue and yellow circles represent A^I and A^{II} sites respectively. The green circles are oxygen atoms and O4 is the free oxygen.(For interpretation of the references to colour in this figure legend, the reader is referred to the web version of this article.)

larger Ce^{3+} cations have substituted Y^{3+} ($r_{Ce3+} = 1.01$ Å, $r_{Y3+} = 0.9$ Å when CN = 6) without changing the structural symmetries. Previous studies about the crystal structure of $Sr_2Y_8(SiO_4)_6O_2$ indicate Y^{3+} occupy two different types of cationic sites A^I and A^{II} with Wycoff symbols 4*f* and 6*h* respectively. A^I site coordinates with nine oxygen atoms and constructs a tricapped trigonal-prismatic geometry; A^{II} site coordinates by seven oxygen atoms including one free-oxygen O4 to form irregular polyhedra with pentagonal bipyramidal geometry (Fig. 5). The free oxygen is underbonded and closely bonded to A^{II} cation [17,18]. Since Y^{3+} is substituted by Ce^{3+}, it is believed that Ce^{3+} also occupies two cationic sites. According to Blasse's theory, the cationic site with free-oxygen nearby prefers to accommodate cations with high charge or small radius in order to compensate the underbonded valence [19]. Therefore, in the present study, larger Ce^{3+} cations are more likely to occupy A^I sites rather than A^{II} sites and this preference of occupancy will influence on the photoluminescent properties.

The PL and PLE of $Sr_2Y_{8-x}Ce_x(SiO_4)_6O_2$ ($x = 0.01$, 0.05 and 0.1) translucent ceramics at room temperature are shown in Fig. 6. All the broad bands in these spectra correspond to the electronic transitions between 4*f* and 5*d* shells of Ce^{3+} cations. In the PL spectra of $Sr_2Y_{7.99}Ce_{0.01}(SiO_4)_6O_2$ excited by 320 nm, single band appears at 391 nm, which should be ascribed to the transition from the lowest 5*d* state to 4*f* states at one crystallographic site. Although Ce^{3+} emission should be doublet as 4*f* states consist of two levels ^2F_J ($J = 7/2$ and 5/2), the single emission band in silicate apatite have been observed by Lammers and Blasse [20] due to the structural disorder. Moreover, a shoulder at 424 nm becomes obvious in the PL spectra excited by 295 nm, which is related to the other crystallographic site. Based on that fact that Ce^{3+} ions prefer occupying the A^I sites as discussed above, the intense broad band at 391 nm should correspond to electronic transitions of Ce^{3+} at A^I sites (Ce^{3+}(I)) and the shoulder at 424 nm corresponds to the small portion of Ce^{3+} occupying A^{II} sites (Ce^{3+}(II)). This designation is consistent with the results from the PLE spectra. When the emission is monitored at 391 nm, single band at 320 nm appears in the PLE spectra which corresponds to the transition from the 4*f* to 5*d* state of Ce^{3+}(I). However, a shoulder at 295 nm become pronounced if the emission is fixed at 424 nm because the overlap of emissions from Ce^{3+}(I) and Ce^{3+}(II). Therefore, Ce^{3+}(II) is excited by incident light with 295 nm wavelength and its lower intensity is due to fewer Ce^{3+}(II) than Ce^{3+}(I) in the material. In all the PL and PLE spectra of $Sr_2Y_{7.95}Ce_{0.05}(SiO_4)_6O_2$ (Fig. 6c and d), the characteristic bands related to Ce^{3+}(II) gain more intensity as compared to $Sr_2Y_{7.99}Ce_{0.01}(SiO_4)_6O_2$ though the intensities still lower than those of Ce^{3+}(I). It indicates that the site preference of Ce^{3+} to A^I sites maintains and the amount of Ce^{3+} cations occupying A^{II} sites increases when the cerium doping concentration is increased. As the spectra are deconvoluted by two-peak Gaussian fitting, it is obvious that the characteristic bands from Ce^{3+}(I) and Ce^{3+}(II) are overlapped when the sample is excited at 295 nm or the emission is monitored at 424 nm. That is why the PL excited at 295 nm and PLE monitored at 424 nm exhibit both Ce^{3+}(I) and Ce^{3+}(II) features. However, it is difficult to explain the existence of the band related to Ce^{3+}(II) in PL spectra when the excitation wavelength is 320 nm, since the overlap is limited. Most reasonable explanation for this phenomenon is the existence of energy transfer from Ce^{3+}(I) to Ce^{3+}(II). Part of the energy absorbed by Ce^{3+}(I) is transferred to Ce^{3+}(II), leading to the appearance of Ce^{3+}(II) band in PL when only Ce^{3+}(I) are excited. For $Sr_2Y_{7.9}Ce_{0.1}(SiO_4)_6O_2$ ceramic, the PLE spectra monitored at 391 and 424 nm are similar to those of $Sr_2Y_{7.95}Ce_{0.05}(SiO_4)_6O_2$, in line with the occupational preference of Ce^{3+} to A^I. The Ce^{3+}(II) band (424 nm) becomes more intense than the one of Ce^{3+}(I) (391 nm) in the PL spectra when only Ce^{3+}(I) is excited (320 nm), which further substantiates the existence of the energy transfer from Ce^{3+}(I) to Ce^{3+}(II). The statistical distances between Ce^{3+} cations are decreased with the increase of the cerium doping concentration and subsequently the probability of the energy transfer is increased, leading to high intensity of Ce^{3+}(I) band in PL spectra.

According to the analysis of the PL and PLE spectra, the energy levels of Ce^{3+} at A^I and A^{II} sites are demonstrated by the configurational coordinate model (Fig. 7). The parabolas of the lowest 5*d* states of Ce^{3+}(I) and Ce^{3+}(II) are different due to the coordination environment. The 4*f* states are well shielded by outer electrons and can be considered as constant in different environments [21], so the parabolas of Ce^{3+}(I) and Ce^{3+}(II) are the same in the model. Based on the PL and PLE spectra, the stokes shifts of Ce^{3+}(I) and Ce^{3+}(II) are 5675 and 10,313 cm^{-1}. The larger stokes shift of Ce^{3+}(II) than Ce^{3+}(I) can be explained by the larger parabola offset ΔR for Ce^{3+}(II), which indicates that the environment around A^{II} site is less stiff than that around A^I. Moreover, the parabola of Ce^{3+}(II) lies at lower position than that of Ce^{3+}(I), which could be attributed to the nephelauxetic effect and the crystal filed [21]. The free-oxygen closely bonded to A^{II} site not only increases the covalency of the Ce^{3+}–O bond but also enhances the crystal field at A^{II} site, both of which could lower the 5*d* levels of Ce^{3+}(II).

To further study the photoluminescence mechanisms, the time resolved photoluminescence decay profiles of $Sr_2Y_{8-x}Ce_x(SiO_4)_6O_2$

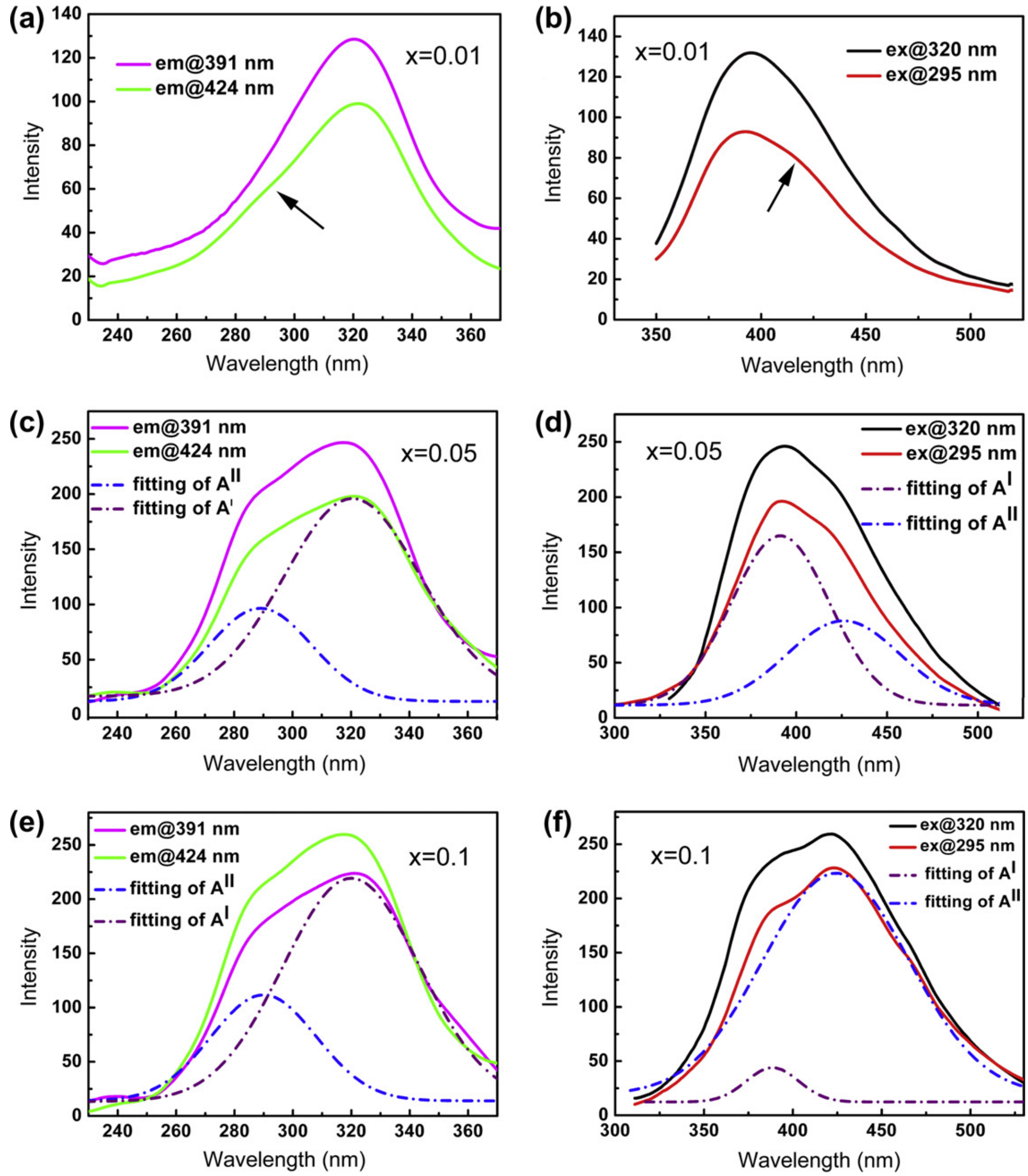

Fig. 6. PL and PLE spectra and the results of Gaussian fittings. (a) PLE of $Sr_2Y_{7.99}Ce_{0.01}(SiO_4)_6O_2$; (b) PL and Gaussian fittings of $Sr_2Y_{7.99}Ce_{0.01}(SiO_4)_6O_2$; (c) PLE and Gaussian fittings of $Sr_2Y_{7.95}Ce_{0.05}(SiO_4)_6O_2$; (d) PL and Gaussian fittings of $Sr_2Y_{7.95}Ce_{0.05}(SiO_4)_6O_2$; (e) PLE and Gaussian fittings of $Sr_2Y_{7.9}Ce_{0.1}(SiO_4)_6O_2$; (f) PL and Gaussian fittings of $Sr_2Y_{7.9}Ce_{0.1}(SiO_4)_6O_2$. The shoulders corresponding to Ce^{3+}(II) site in (a) and (b) are indicated by arrows.

(x = 0.01, 0.05 and 0.1) ceramics are measured (Fig. 8). Though the emission bands of Ce^{3+}(I) and Ce^{3+}(II) are peaked around 391 and 424 nm according to the analysis of PL and PLE, the emissions related to Ce^{3+}(I) and Ce^{3+}(II) for the decay measurements are monitored at 350 and 435 nm respectively in order to minimize the influence of the spectral overlap of Ce^{3+}(I) and Ce^{3+}(II) emissions. The decay times of Ce^{3+}(I) are always faster than those of Ce^{3+}(II) due to the energy transfer from Ce^{3+}(I) to Ce^{3+}(II). The differences between the decay profiles of Ce^{3+}(I) and Ce^{3+}(II) are enlarged with the increase of the Ce^{3+} concentration, because the energy transfer process becomes more pronounced in higher Ce^{3+} concentration.

Since the transition from Ce^{3+} 5d to 4f states is parity allowed and the emission of Ce^{3+}(I) overlaps with the excitation spectra of Ce^{3+}(II), the energy transfer should be dipole–dipole interaction with Ce^{3+}(I) acting as the donors and Ce^{3+}(II) as the acceptors. Therefore, the variation of the emission intensity of Ce^{3+}(I) as a function of time can be expressed as [22,23]:

$$I_{\mathrm{I}} = I_0^{\mathrm{I}} \exp(-t/\tau_0 - Ct^{1/2}) \tag{1}$$

$$C = \frac{4}{3}\pi^{3/2} R_{\mathrm{II}}^3 n_{\mathrm{a}}^{\mathrm{II}} \Big/ (\tau_0)^{1/2} \tag{2}$$

where τ_0 is the intrinsic radiative decay time of Ce^{3+}(I), $n_{\mathrm{a}}^{\mathrm{II}}$ is population of Ce^{3+}(II) in the unit volume, R_{II} is the critical distances of the energy transfer process from Ce^{3+}(I) to Ce^{3+}(II).

All of the decay profiles are global fitted by Eq. (1). The value τ_0 is set as the shared value since the donors Ce^{3+}(I) are the same for

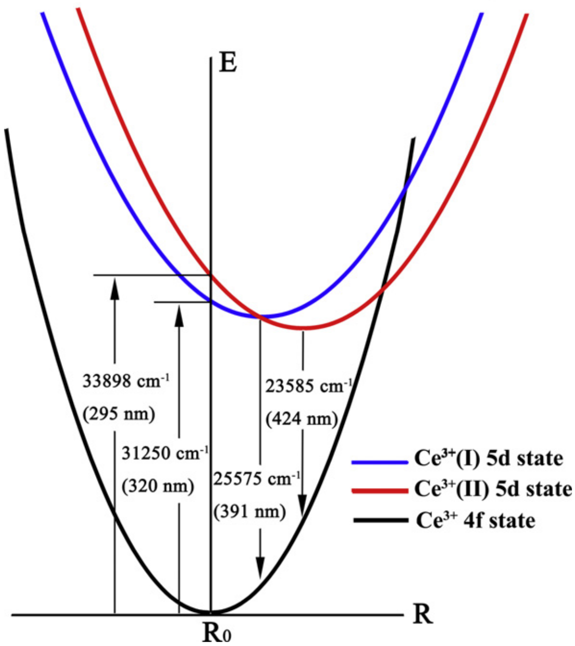

Fig. 7. The configurational coordinate model of the energy levels for Ce^{3+}(I) and Ce^{3+}(II). Blue and red parabola represent the 5*d* states of Ce^{3+}(I) and Ce^{3+}(II) respectively. The 4*f* states (black parabola) of Ce^{3+}(I) and Ce^{3+}(II) are the same because 4*f* are well shielded by outer shell electrons.

all three samples. Subsequently the intrinsic radiative decay time and the parameter *C* for samples with different Ce^{3+} concentrations are obtained (Table 1). The intrinsic radiative decay time for Ce^{3+}(I) turns out to be 34.4 ns which is comparable to the values of other Ce^{3+} doped apatites [24–26]. The *C* values can be considered as a parameter to measure the energy transfer process. In the current case, τ_0 and R_{II} are fixed for all the three samples. Thus, the parameter *C* is proportional to the population density of Ce^{3+}(II) according to Eq. (2). With the increase of the Ce^{3+} concentration, the population density of Ce^{3+}(II) as well as the value of parameter C is also increased. Therefore, the energy transfer process is enhanced and the decay becomes faster in the samples with higher Ce^{3+} concentration. However, the population density of Ce^{3+}(II) does not vary linearly with the Ce^{3+} concentration, which may be due to the occupancy preference of Ce^{3+} as discussed above. The Ce^{3+} cations prefer entering Ce^{3+}(I) sites to Ce^{3+}(II) sites. Consequently, the increase of population density of Ce^{3+}(II) is not as much as that of the Ce^{3+} concentration.

The mean decay times at emission 350 nm for these translucent ceramics can be roughly estimated by:

$$\tau_m = \int_0^\infty tI(t)\mathrm{d}t \Big/ \int_0^\infty I(t)\mathrm{d}t \tag{3}$$

where *I(t)* is obtained from Eq. (1). And the results are 13.5, 13.28 and 11.9 ns for $Sr_2Y_{7.99}Ce_{0.01}(SiO_4)_6O_2$, $Sr_2Y_{7.95}Ce_{0.05}(SiO_4)_6O_2$ and $Sr_2Y_{7.9}Ce_{0.1}(SiO_4)_6O_2$ respectively. All the average lifetimes are below 20 ns, which are relatively short in comparison with other Ce^{3+} doped materials [26,27]. It suggests that fast responses are probable when these translucent ceramics are implemented as scintillators, and detailed studies of these ceramics with X-ray and gamma-ray irradiation are under going.

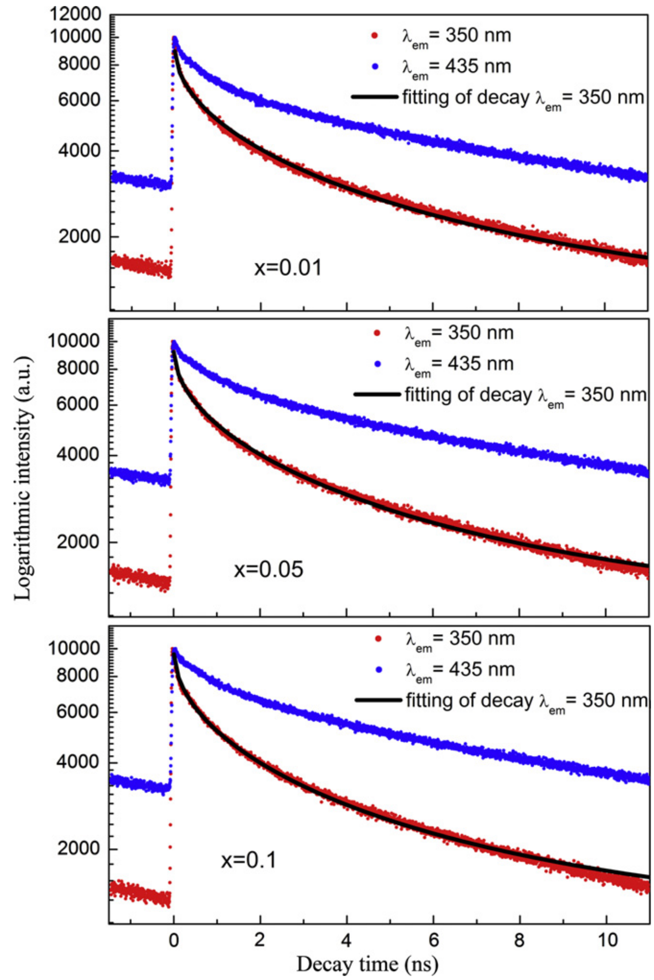

Fig. 8. The emission decay profiles of Ce^{3+}(I) (monitored at 370 nm, red color) and Ce^{3+}(II) (monitored at 435 nm, blue color). The emission of Ce^{3+}(II) decays slower than the that of Ce^{3+}(I) in each sample. The global fitting curves are shown in black solid line.

Table 1
The global fitting results of the decay profiles of Ce^{3+}(I) emission at 350 nm in $Sr_2Y_{8-x}Ce_x(SiO_4)_6O_2$.

x	*C*	τ_0 (ns)	R^2
0.01	0.6525	34.4	0.9971
0.05	0.6787		
0.1	0.7213		

4. Conclusions

Spark plasma sintering is applied to condense the luminescent material Ce^{3+}:$Sr_2Y_8(SiO_4)_6O_2$ into translucent ceramics. The grains in the ceramics are closely compacted and no entrapped pores are found under SEM. Ce^{3+} cations occupy two cationic sites A^I and A^{II} with different coordination environments, which results in different photoluminescent features in the spectroscopic analysis. The energy levels of Ce^{3+} at A^I and A^{II} sites are demonstrated by the configurational coordinate model based on the studies of the photoluminescence spectra. The energy transfer from Ce^{3+}(I) to Ce^{3+}(II) is revealed from the photoluminescence spectra and confirmed by the decay profiles. The global fitting results of Ce^{3+}(I) decay profiles show that the intrinsic decay time of Ce^{3+}(I) is 34.4 ns. With the increase of Ce^{3+} concentration, the energy transfer process becomes more pronounced due to higher population density of the acceptor Ce^{3+}(II).

Acknowledgment

We are thankful for financial support from the NTU Research Scholarship and NTU AcRF grant (RG11/04).

References

[1] A. Ikesue, T. Kinoshita, K. Kamata, K. Yoshida, J. Am. Ceram. Soc. 78 (1995) 1033–1040.
[2] G.C. Wei, J. Eur. Ceram. Soc. 29 (2009) 237–244.
[3] C. Greskovich, S. Duclos, Annu. Rev. Mater. Sci. 27 (1997) 69–88.
[4] K. Hayashi, O. Kobayashi, S. Toyoda, K. Morinaga, Mater. Trans., JIM 32 (1991) 1024–1029.
[5] J. Sanghera, W. Kim, C. Baker, G. Villalobos, J. Frantz, B. Shaw, A. Lutz, B. Sadowski, R. Miklos, M. Hunt, F. Kung, I. Aggarwal, Opt. Mater. 33 (2011) 670–674.
[6] S.H. Lee, E.R. Kupp, A.J. Stevenson, J.M. Anderson, G.L. Messing, X. Li, E.C. Dickey, J.Q. Dumm, V.K. Simonaitis-Castillo, G.J. Quarles, J. Am. Ceram. Soc. 92 (2009) 1456–1463.
[7] A.C. Bravo, L. Longuet, D. Autissier, J.F. Balumard, P. Vissie, J.L. Longuet, Opt. Mater. 31 (2009) 734–739.
[8] M. Omori, Mater. Sci. Eng., A 287 (2000) 183–188.
[9] R. Apetz, M.P.B. van Bruggen, J. Am. Ceram. Soc. 86 (2003) 480–486.
[10] Y.Q. Shen, J.L. Xu, A. Tok, D.Y. Tang, K.A. Khor, Z.L. Dong, J. Am. Ceram. Soc. 93 (2010) 3060–3063.
[11] A. Lempicki, C. Brecher, H. Lingertat, S.R. Miller, J. Glodo, V.K. Sarin, IEEE Nucl. Sci. 55 (2008) 1148–1151.
[12] D.J. Wisniewski, L.A. Boatner, J.S. Neal, G.E. Jellison, J.O. Ramey, A. North, M. Wisniewska, A.E. Payzant, J.Y. Howe, A. Lempicki, C. Brecher, J. Glodo, IEEE Nucl. Sci. 55 (2008) 1501–1508.
[13] E.V. van Loef, Y.M. Wang, S.R. Miller, C. Brecher, W.H. Rhodes, G. Baldoni, S. Topping, H. Lingertat, V.K. Sarin, K.S. Shah, Opt. Mater. 33 (2010) 84–90.
[14] Z.F. Wang, W.P. Zhang, L. Lin, B.G. You, Y.B. Fu, M. Yin, Opt. Mater. 30 (2008) 1484–1488.
[15] Y. Shi, Q.W. Chen, J.L. Shi, Opt. Mater. 31 (2009) 729–733.
[16] B. Francois, M. Navizet, J. Rebreyend, C. Won, US Patent No. 4988882, 1991.
[17] Y.Q. Shen, A. Tok, D.Y. Tang, Z.L. Dong, J. Am. Ceram. Soc. 93 (2010) 1176–1182.
[18] I.D. Brown, The chemical bond in inorganic chemistry: the bond valence model, Oxford University Press, Oxford, 2006.
[19] G. Blasse, J. Solid State Chem. 14 (1975) 181–184.
[20] M.J.J. Lammers, G. Blasse, J. Electrochem. Soc. 134 (1987) 2068–2072.
[21] G. Blasse, B.C. Grabmajer, Luminescent materials, Springer-Verlag, Berlin, 1994.
[22] K.B. Eisenthal, S. Siegel, J. Chem. Phys. 41 (1964) 652–655.
[23] G. Blasse, Phys. Lett. A 28 (1968) 444–445.
[24] J.H. Zhang, H.B. Liang, Q. Su, J. Phys. D: Appl. Phys. 42 (2009) 105110.
[25] Q. Zeng, H.B. Liang, G.B. Zhang, M.D. Birowosuto, Z.F. Tian, H.H. Lin, Y.B. Fu, P. Dorenbos, Q. Su, J. Phys.: Condens. Matter 18 (2006) 9549.
[26] J.H. Zhang, H.B. Liang, R.J. Yu, H.B. Yuan, Q. Su, Mater. Chem. Phys. 114 (2009) 242–246.
[27] J. Sokolnicki, M. Guzik, Opt. Mater. 31 (2009) 826–830.